Overview of Rotor Hover Performance Capabilities at Low Reynolds Number for Mars Exploration

Witold J. F. Koning,[1] B. Natalia Perez Perez,[2] Haley V. Cummings,[3] Ethan A. Romander,[4] and Wayne Johnson[5]

NASA Ames Research Center, Moffett Field, California 94035

ABSTRACT

The Evolutionary aLgorithm for Iterative Studies of Aeromechanics (ELISA) software was developed in support of the Rotorcraft Optimization for the Advancement of Mars eXploration (ROAMX) project. ELISA was developed to enable aerodynamic rotor hover optimization for low Reynolds number flows in the Mars atmosphere. ELISA comprises two modules. The first module is dedicated to airfoil optimization and allows for the creation of multi-objective Pareto-optimal (PO) airfoil sets with the airfoil performance evaluation performed using the CFD code OVERFLOW. The second module is dedicated to rotor hover performance optimization and generates multi-objective PO rotor sets with the rotor performance evaluation performed using the comprehensive analysis code CAMRAD II. This paper presents recent updates to the ELISA optimization toolset. The airfoil module now includes variation in section Reynolds number, alongside simultaneous maximization of section lift and minimization of section drag. Consequently, the rotor optimization module can query PO airfoil sets (as a function of section lift, drag, and Reynolds number) and generate PO C81 airfoil decks tailored to specific Reynolds numbers; this eliminates the need for adequate initial chord guesses and allows for arbitrary rotor solidities to be studied. Furthermore, the rotor optimization procedure has been extended to incorporate a third dimension, alongside maximization of blade loading and minimization of rotor power. This enables optimization across a relevant density range on Mars, resulting in the lowest power rotor hover geometry (for each attainable blade loading and each density). The goal of this work is to present the relevance of recent updates to the ELISA optimization toolset, by demonstrating full rotor hover optimization using unconventional airfoils across a practical Mars density range, and by presenting various optimum solutions involving variable number of blades along with unconstrained solidity in the Mars atmosphere.

NOTATION

A	rotor disk area, m^2
c	chord, m
c_d	section drag coefficient, $D/(0.5\rho_\infty U_\infty^2 c)$
c_l	section lift coefficient, $L/(0.5\rho_\infty U_\infty^2 c)$
C_P	rotor power coefficient, $P/(\rho_\infty A(\Omega R)^3)$
C_T	rotor thrust coefficient, $T/(\rho_\infty A(\Omega R)^2)$
D	section aerodynamic drag force, N/m
f	fitness
e	exponent value for Re fitness calculation
FM	rotor hover figure of merit, $T\sqrt{T/(2\rho_\infty A)}/P$
L	section aerodynamic lift force, N/m
M	Mach number
N	number of blades
P	rotorcraft power, W
r	rotor radial coordinate, m
R	rotor radius, m; range, km
Re	chord-based Reynolds number, $\rho_\infty U_\infty c/\mu$
t	airfoil thickness, m
T	rotor thrust, N
U	velocity, m/s
x	local x coordinate (along chord)
y	local y coordinate (perpendicular to chord)
y^+	dimensionless wall distance
α	angle of attack, deg
θ	rotor twist, deg
μ	dynamic viscosity, Ns/m^2
ρ	density, kg/m^3
σ	thrust-weighted solidity, $\frac{3N}{\pi R}\int_0^R cr^2 dr$
Ω	rotor rotational speed, rad/s

Subscripts

cr	coaxial rotor
d	drag
e	experimental result
l	lift
max	maximum
min	minimum
sr	single rotor

[1] Aerospace Engineer, Aeromechanics Branch, Science and Technology Corporation; witold.koning@nasa.gov.
[2] Aerospace Engineer, Aeromechanics Branch, Science and Technology Corporation; natalia.perezperez@nasa.gov.
[3] Aerospace Engineer, Aeromechanics Branch, haley.cummings@nasa.gov.
[4] Aerospace Engineer, Aeromechanics Branch; ethan.romander@nasa.gov.
[5] Aerospace Engineer, Aeromechanics Branch; wayne.johnson@nasa.gov.

Presented at the 50th European Rotorcraft Forum, Marseille, France, Sept. 10-12, 2024.

tip	condition at the blade tip
∞	freestream condition
$*$	reference value

Acronyms

CA	Comprehensive Analysis
DRT	Dual Rotor Test
ELISA	Evolutionary aLgorithm for Iterative Studies of Aeromechanics
EDM1	Engineering Design Model 1
GA	Genetic Algorithm
LE	Leading Edge
MOGA	Multi-Objective Genetic Algorithm
PO	Pareto-optimal
ROAMX	Rotor Optimization for the Advancement of Mars eXploration
SRH	Sample Recovery Helicopter
TE	Trailing edge
TRT	Transonic Rotor Test
UNS	Unsteady Navier-Stokes

INTRODUCTION

The success of the Mars Helicopter Ingenuity has inspired efforts to improve fundamental understanding of compressible, low Reynolds number aerodynamics and rotor performance (at very low densities). Studies have focused on optimizing unconventional airfoils, revealing significant possible advancements in sectional aerodynamic airfoil performance [1,2]. These airfoils were integrated into the Mars Science Helicopter conceptual design, demonstrating improved rotor efficiency compared to Ingenuity and revealing the potential of employing ultra-thin rotor blades for Mars exploration [3,4]. The "Evolutionary aLgorithm for Iterative Studies of Aeromechanics" (ELISA) optimization toolset was developed under the Rotorcraft Optimization for the Advancement of Mars eXploration (ROAMX) with the goal of presenting one of the first fully hover-optimized rotors for Mars exploration. ELISA was introduced in Ref. [5] to enable comprehensive airfoil and rotor optimization studies tailored for Mars environments.

This paper builds on previous work and showcases the capabilities of the expanded ELISA toolset. It presents relevant use cases focusing on the optimization of Ingenuity-class single rotors. First, the generation of a Pareto-optimal (PO) airfoil set (e.g., no objective function can be improved without degrading any other objective function) across a relevant density range for Mars rotorcraft exploration is presented. Second, a rotor optimization across this density range is presented next to a study on the effect of blade number and solidity variation. The paper concludes with a discussion of relevant findings and an outline of future research objectives.

THE ELISA OPTIMIZATION TOOLSET

ELISA was developed to enable aerodynamic rotor hover optimization for low Reynolds number flows in the Mars atmosphere. The first module of the algorithm facilitates (un)conventional airfoil parameterization and multi-objective optimization of airfoil geometry using the CFD code OVERFLOW. This includes simultaneous maximization of section lift, minimization of section drag, and optionally, variation of section Reynolds number or section thickness. The resulting PO airfoil sets are converted to a set of PO C81 airfoil decks, providing the lowest drag airfoil geometry for each angle of attack (with a possible section Reynolds number or section thickness constraint). This removes the need for arbitrary airfoil selection in the rotor optimization, which is possible due to the section lift of the PO airfoil set still being proportional to angle of attack, allowing PO airfoil data to be expressed in an airfoil deck format. This approach restricts angle of attack variation along the blade span with variation in blade azimuth. In the case that unsteady aerodynamics are present in hover, the user can specify the maximum allowable angle of attack variation with blade azimuth. Furthermore, section Reynolds number or section thickness can be used as additional parameter in creating the PO airfoil decks.

The second module facilitates rotor geometry optimization using the comprehensive analysis code CAMRAD II, aiming to simultaneously maximize rotor blade loading and minimize rotor power. The result is a PO rotor set, providing the lowest rotor power for each attainable rotor blade loading. If included in the airfoil optimization, adjustments to the airfoil thickness or Reynolds number can be modified post airfoil optimization. This allows for subsequent adjustment of blade thickness to conform to external structural requirements, or for variation of sectional Reynolds numbers to accommodate factors such as varying operating density and changing chord lengths.

Subsequent chapters will describe the improvements to the algorithm presented in this work. The reader is referred to Ref. [5] for a more fundamental description of the ELISA optimization toolset and components. A summary is presented below for the benefit of the reader.

Updates to the ELISA Optimization Toolset

The airfoil optimization allows for variation in section Reynolds number (instead of section thickness) for a fixed Mach number. This eliminates the need for initial chord guess (and rotor solidity) during rotor optimization, provided the Reynolds number range in the PO airfoil sets is broad enough to cover the chord constraints for the chosen operating condition range. Although generating a high-quality PO airfoil set can be computationally expensive, these PO airfoil sets can be reused for other studies as long as the desired Mach number is present along the span of the rotor. The fitness calculation for section lift and drag is shown in Eq. (1)

$$f_1 = \left(1 - \frac{c_l}{c_l^*}\right)^2, \qquad f_2 = \left(1 - \frac{c_d^*}{c_d}\right)^2 \tag{1}$$

where c_l^* and c_d^* are (unattainable) reference values. The fitness calculation for the Reynolds number is provided by Eq. (2)

$$f_3 = \frac{\log_{10}(Re) - e_{min}}{(e_{max} - e_{min})} \tag{2}$$

with $10^{e_{min}} \leq Re \leq 10^{e_{max}}$. These boundaries can be chosen to either limit the search space by calculating the expected Reynolds number range for each radial station (together with chord and density constraints during rotor optimization) or can be used to limit the Reynolds number range for which a particular airfoil performance function evaluation is applicable. This fitness calculation is used instead of the thickness fitness (as used in Ref. [5]). The fitness functions for rotor optimization follow the same approach for blade loading, rotor power, and density. The square in the fitness terms in Eq. (1) is optional, as is the choice to evaluate f_3 using a logarithm with base 10.

All airfoil parameterization types can now include a minimum prescribed thickness to facilitate generating practical blade geometries. This requirement arises because section thickness cannot be chosen as an objective alongside section Reynolds number. Adding a fourth objective would introduce additional complexity and will get prohibitively expensive when using high-fidelity CFD for the airfoil function evaluation.

Variation of a third variable for rotor optimization can now also be selected, which is useful for varying operating conditions (e.g., density, tip Mach number, or rotor radius) that could vary the Reynolds number, alongside planform changes. Currently, only an option for atmospheric density variation is implemented, but other parameters are planned to be added in the future.

Next to the ROAMX airfoil parameterization [5], which is primarily used for unconventional airfoil parametrization, the user can now also choose PARSEC airfoil parametrization [6]. This option can aid studies into conventional (tear drop) airfoil usage at low or conventional Reynolds numbers.

Several convenience features are also implemented to facilitate studies at higher rotor solidities. For example, the rotor optimization procedure detects instances where a particular planform has overlapping blades and can optionally discard these rotor geometries. The root section is particularly at risk of creating overlapping blades, depending on the root cutout location, number of blades, and the blade planform.

Continuum-type fluid dynamics (and Newtonian fluid assumptions) can become invalid at subsonic Mach numbers at the lower end of the practical Reynolds number regime for Mars rotor applications. As presented by Ref. [7], the boundary between continuum flow and the interaction phase (the phase before the onset of slip flow and true free molecule flow) can be estimated by Eq. (3)

$$\sqrt{Re} = 100M \tag{3}$$

The code uses Eq. (3) to approximate the fluid dynamic realm along the blade span, to verify the validity of airfoil performance calculations, particularly in the lower density ranges relevant to Mars rotorcraft.

User Inputs

The first set of user inputs requires the primary flight conditions for the rotor and includes the tip Mach number, M_{tip}, and location-based conditions (atmospheric density, temperature, dynamic viscosity). The objective of the code is rotor hover optimization, so for this reason, no tradeoffs with cruise speed will be considered and M_{tip} is therefore specified as an input. This avoids optimization up to drag-divergence Mach numbers (and thereby strongly limiting any forward flight speed).

User input for the rotor module includes the rotor radius, rotor root cutout, and the radial stations at which airfoil optimization is to be performed. The rotor chord and twist can both be optimized and are either not parameterized (individual values per radial station), or use a linear, quadratic, or cubic Bézier curve for their parameterization. The rotor optimization uses dual or triple objectives: maximization of blade loading, C_T/σ, and simultaneous minimization of rotor power, C_P/σ, and optionally a variation of a third variable, demonstrated here with atmospheric density, ρ. A minimum C_T/C_P ratio is set to avoid generating designs at very low lift or during blade stall, but low-thrust solutions can be kept in the PO rotor selection procedure if so desired.

The airfoil optimization is performed for each radial station in parallel, prior to the rotor optimization. The airfoil parameterization can be set to `roamx` (dual objectives: maximization of c_l and minimization of c_d) or `roamx3` (`roamx` objectives and variation of a structural metric or Reynolds number) or their PARSEC equivalents (`parsec` or `parsec3`). In the current work only section Reynolds number variation is pursued. A desired minimum c_l/c_d threshold is set to avoid optimizing for stalled conditions (which are non-physical in 2D and of limited use), but optionally low c_l values can be included in the PO airfoil selection procedure.

Airfoil Optimization: Function Evaluation in OVERFLOW

All airfoil performance function evaluations are performed using 2D Computational Fluid Dynamics (CFD) with structured grids and solved using the implicit, compressible Navier-Stokes solver OVERFLOW 2.3d [8,9]. Inviscid fluxes are computed using the HLLE++ flux schemes with a 5th-order WENOM upwind reconstruction approach for high spatial accuracy with low numerical dissipation [10]. Viscous fluxes are computed using 2nd-order central differencing, as are grid metric terms. Time advance uses a 2nd-order backward differencing scheme, with a dual time-stepping approach as described in Refs. [11,12].

All analyses presented in this work are performed using laminar Unsteady Navier-Stokes (UNS) equations and no turbulence model is employed (as discussed in Refs. [5,13]). Simulations in the present work are set up using a set of coarse timesteps at first to remove the initial transients before starting the time-accurate runs. During post processing, the transients of the time-accurate part of the simulations are evaluated to remove them from the computation of the mean and to compute the corresponding confidence intervals, according to Ref. [14].

The location of the leading edge (LE), possible discontinuities along the airfoil shape, and trailing edge (TE) are provided to the grid generation script which automatically refines the chordwise spacing around discontinuities in the grid. The basic grid generation of the airfoils is described in [13,15], but the maximum chordwise and off body separation was set at $1\%c$ to reduce the grid size and computation time. The spacing normal to the airfoil surface places the first point at $y^+ < 1$. Body-fitted grids model each airfoil and are embedded in a Cartesian background mesh that extends 200 chord lengths from the airfoil. Flow variables are interpolated between grids at the overset boundaries in a manner that preserves the full accuracy of the solver.

The grids place approximately 800 points around the airfoil with the points clustered to ensure geometric fidelity and accurate capture of flow gradients. Grid stretching ratios do not exceed 10% in any directions. Airfoil surfaces are modeled with a viscous boundary condition, and the far field boundaries are modeled using a freestream characteristic boundary condition.

The airfoil function evaluation is the constraining element of the ELISA workflow. To alleviate this computational constraint, the airfoil optimization code automatically distributes each chromosome in the evolutionary algorithm to a dedicated node on the Pleiades Supercomputer at NASA Ames Research Center to compute the whole generational fitness in parallel to efficiently advance the solutions.

Rotor Optimization: Function Evaluation in CAMRAD II

All rotor performance function evaluations are performed using the Comprehensive Analysis (CA) code CAMRAD II [16]. The CA model is set up to use the generated PO-C81 tables and predict the corresponding rotor performance. The CAMRAD II aerodynamic model for the rotor blade is based on lifting-line theory, using steady two-dimensional airfoil characteristics, a vortex wake model, and additional models for unsteady flow (attached flow and dynamic stall) and yawed/swept flow. Effects of compressibility (Mach numbers) and viscosity (Reynolds number, stall, and drag) enter through airfoil table data: lift, drag, and moment coefficients of two-dimensional sections as function of angle of attack and Mach number, for the appropriate chord and atmosphere conditions (density, temperature) to have correct Reynolds number variation with Mach number.

PARETO-OPTIMAL AIRFOIL SET GENERATION

The rotor optimization studies presented in this paper all use the same PO airfoil sets described in this chapter. The ROAMX rotor (see Ref. [5]) was used as a baseline geometry to inform the choices for the basic constraints. This includes the radial stations at which the airfoils are optimized, the required sectional thickness, and the tip Mach number ($M_{tip} = 0.80$).

The potential of unconventional airfoils (e.g., thin airfoils with sharp leading edges and/or features) was investigated in prior work [1,2,17]. To more effectively evaluate unconventional airfoil shapes while keeping the number of decision variables to a minimum, the ROAMX parameterization [5] was developed. Similar to the ROAMX rotor, the `roamx-0201` and `roamx-0202` parameterization schemes are used to obtain efficient compressible low-Reynolds number airfoil geometries, as they are cost-effective in this regime [1,5,17]. An example parameterization for a `roamx-0201` airfoil ('cambered plate') is shown in Figure 1. The `roamx-0201` geometry is specified using three decision variables: angle of attack and the two coordinates of the quadratic Bézier control point. For thicker profiles near the root the `roamx-0202` parameterization is chosen with prescribed thicknesses as shown in Figure 2.

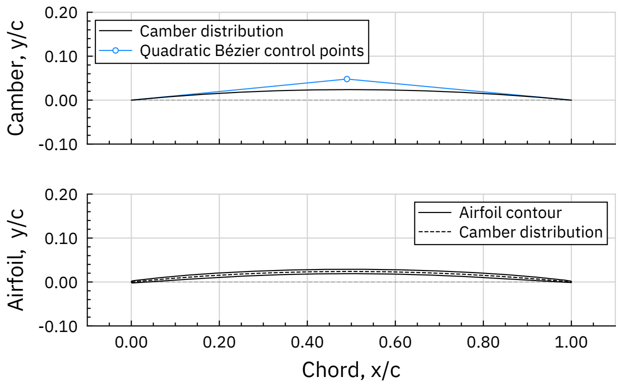

Figure 1. Example `roamx-0201` parameterization.

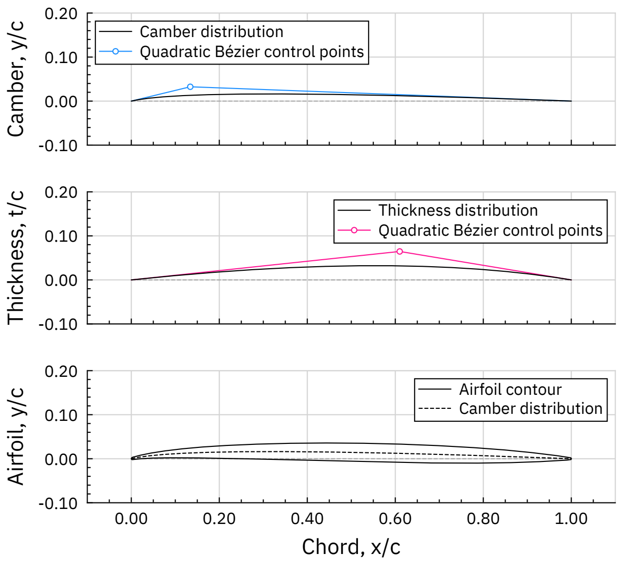

Figure 2. Example `roamx-0202` parameterization.

In contrast to the design of the ROAMX rotor, the airfoil optimization is now performed with section Reynolds number variation. The primary focus was on the outboard airfoil optimization $(r/R \geq 0.50)$, as root airfoils contribute less to rotor hover performance (especially with required relatively thick section generally resulting in poor airfoil efficiencies).

Table 1 shows an overview of the PO airfoil sets, which are all attempting maximization of section lift, minimization of section drag while varying section Reynolds number.

Table 1. Overview of PO airfoil sets parameters

Station	r/R	M	# airfoils	$(t/c)_{min}$	$(c_l/c_d)_{max}$
1	0.0908	0.07	735	0.10	52.40
2	0.2500	0.20	1,000	0.05	69.72
3	0.5000	0.40	3,435	0.01	83.07
4	0.7500	0.60	3,653	0.01	80.24
5	1.0000	0.80	3,208	0.01	64.55

The inboard stations 1 and 2 use `roamx-0202` parameterization with prescribed thickness, while the outboard stations 3 to 5 use `roamx-0201` parameterization with the baseline thickness of $t/c = 1\%$ dictating section thickness. The Reynolds number was varied between $Re = 1{,}000$ (approximate limit of continuum-type fluid dynamics at $M = 0.30$) [7] and $Re = 200{,}000$ (approximate upper limit for assuming laminar flow) [13]. An example PO airfoil set for station 4 is presented in Figure 3. ELISA attempts to homogenize the distribution of the PO geometries in fitness-space to minimize discontinuities along extracted Pareto fronts. The fitness functions and selection procedures are described in Ref. [5].

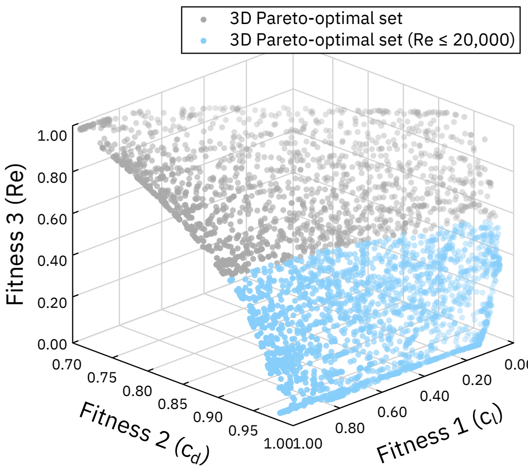

Figure 3. 3D Pareto-optimal airfoil set in fitness-space for station 4 ($M = 0.60$, $1{,}000 \leq Re \leq 200{,}000$).

For an example Reynolds number of $Re = 20{,}000$, the PO airfoil set corresponding to the maximum Reynolds number is highlighted. The extraction procedure of the PO airfoils includes lower Reynolds numbers in a way that includes conservative geometries, since one cannot extract airfoils at an exact Reynolds number. This extraction procedure (from the PO airfoil set presented in Figure 3) is presented in Figure 4.

The first step in the extraction procedure is the application of a $Re \leq 20{,}000$ threshold. This threshold corresponds to a particular Reynolds number of a rotor radial station during the optimization, based on density, velocity or chord. Second, the Pareto-optimality is evaluated in fitness-space, in the Reynolds number plane (i.e., section lift and section drag, see Figure 4), allowing dominant lower Reynolds number individuals to be selected, if need be. Since lower Reynolds numbers are generally conservative estimates, this helps improve the quality of PO C81 decks by increasing the number of geometries the rotor optimization can query afterwards.

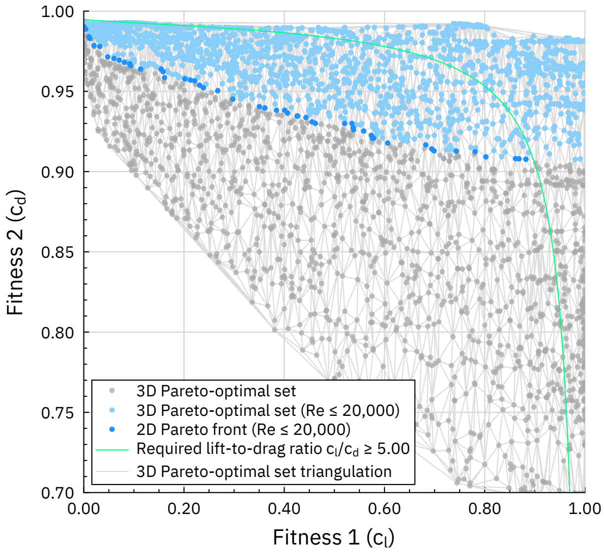

Figure 4. Extracting the Pareto front for $Re \leq 20{,}000$.

Transforming the PO airfoil set in fitness space to aerodynamic performance space presents a more 'human-readable' solution space, as shown in Figure 5. Instead of the section drag, the section lift-to-drag ratio is presented, clearly illustrating how maximum achievable efficiencies for the roamx-0201 parameterization are achievable as a clear function of Reynolds number.

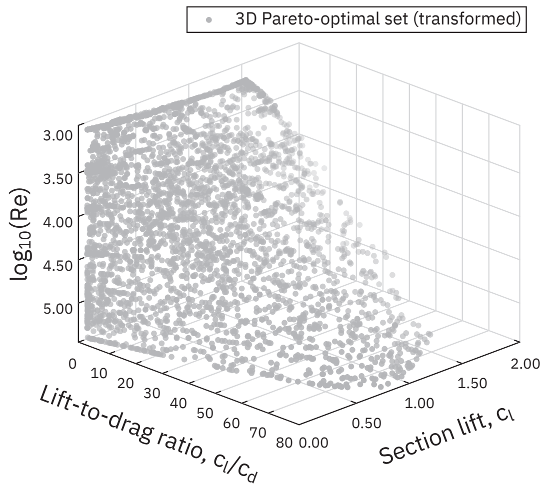

Figure 5. Transformed 3D Pareto-optimal airfoil set for station 4 ($M = 0.60$, $1{,}000 \leq Re \leq 200{,}000$).

Transforming the Pareto front in Figure 4 to aerodynamic integrated coefficients reveals the example set of PO airfoils for $Re \leq 20{,}000$, as shown in Figure 6. The airfoils for select lift coefficients are marked and displayed to illustrate the geometry modification for the PO airfoils as function of section lift.

Evaluating airfoil performance at these conditions is relatively computationally expensive, when compared with more conventional Reynolds numbers. This is primarily due to the possibility of large unsteady structures (mandating an unsteady simulation) and possibly chaotic behavior (mandating sufficient convective time lengths to be simulated to properly characterize the mean flow).

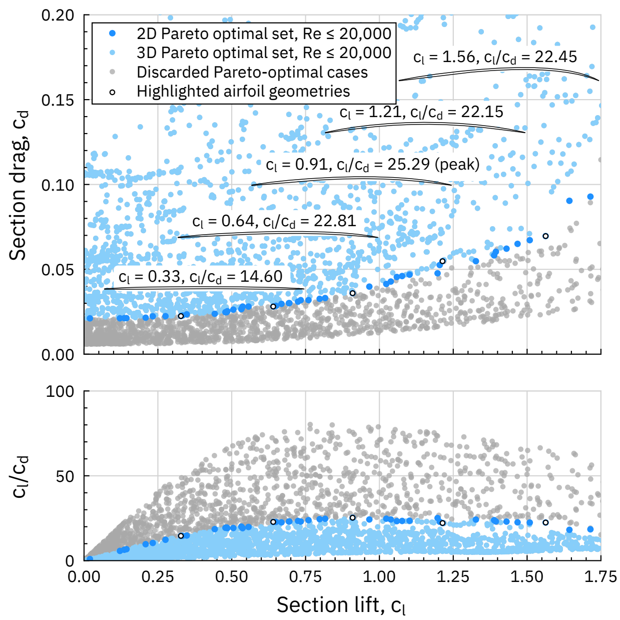

Figure 6. Airfoil performance after extracting the Pareto front for $Re \leq 20{,}000$.

The flowfield around the peak lift-to-drag airfoil from Figure 6 is presented to highlight the complexity of the flow. Figure 7 shows the instantaneous flowfield and the discrete shedding of vortices, while Figure 8 shows the mean flow over the same airfoil.

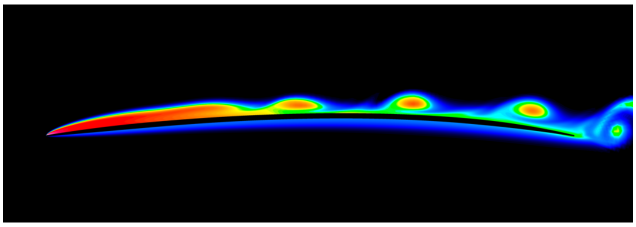

Figure 7. Instantaneous flow field (entropy measure s1).

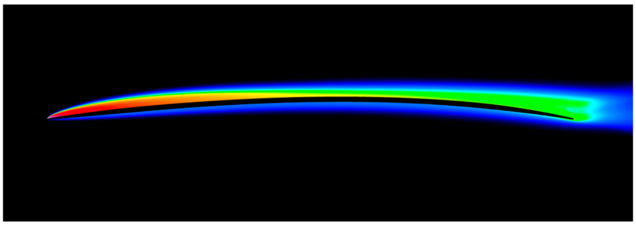

Figure 8. Mean flow field (entropy measure s1).

ROTOR OPTIMIZATION ACROSS MARS DENSITY RANGE

Using the PO airfoil sets obtained, rotor optimization for a single rotor in hover is performed while maximizing blade loading, minimizing rotor power, and varying atmospheric density.

Several experimental Mars studies have been conducted across the density range of $0.010 \leq \rho \leq 0.030$ kg/m^3. These include experimental test campaigns for a single Ingenuity rotor at high tip Mach numbers (Transonic Rotor Test, TRT), a coaxial Ingenuity rotor (Engineering Design Model, EDM1), and a Sample Recovery Helicopter (SRH) test campaign (Dual Rotor Test, DRT). From these tests, peak Figure of Merit performance data has been obtained, as described in Refs. [18,19]. Other concepts have explored the lower end of this density range, as referenced in Refs. [20,21]. To cover a broad range, the allowable density for the rotor optimization is set to $0.005 \leq \rho \leq 0.05$ kg/m^3, which is used here as a practical density range for Mars rotorcraft exploration.

The objective of the present work is to demonstrate optimization for Ingenuity-class single rotors; no coaxial rotors are optimized in this investigation. Therefore, the rotor radius is fixed to that of Ingenuity (and the ROAMX rotor, as optimized): $R = 0.605$ m. This radius is particularly applicable for this study as similarly sized rotors are frequently studied for Mars rotorcraft. Examples, besides Ingenuity, include the Sample Recovery Helicopter rotor [22] and the Mars Science Helicopter rotor concepts [3].

The operating conditions assume a CO_2-rich environment, representative of the Mars atmosphere. Other constraints on the rotor operation are summarized in Table 2. Collective pitch is not varied during the optimization since it is implicitly present in the twist distribution.

Table 2. Primary rotor optimization constraints

Constraint	Value
Root cutout	$r/R = 0.0908$
R	0.605 m
c_{min}	$0.03R$
c_{max}	$0.50R$
θ_{min}	$0.0°$
θ_{max}	$50.0°$
ρ_{min}	0.005 kg/m^3
ρ_{max}	0.050 kg/m^3
M_{tip}	0.80
U_{tip}	186.50 m/s
μ	$1.13 \cdot 10^{-5}$ Ns/m^2
Negative taper enforced	for $R \geq 0.85$
$\Delta\theta/\Delta(r/R)$ twist limiter	$30°$ for $R \geq 0.75$

The planform distributions are parameterized using a cubic Bézier curve and the twist distributions utilize a quadratic Bézier curve, see Ref. [5]. All rotors in the present work are restricted to those which do not have overlapping blade geometries.

Rotor Optimization for Fixed Solidity

The first use case is presented for a rotor optimization with fixed solidity. In addition to the constraints presented in Table 2, the thrust-weighted solidity is held constant at $\sigma = 0.25$ for a 6-bladed rotor. The PO rotor set in fitness-space is shown in Figure 9.

Figure 10 shows the PO rotor set expressed as Figure of Merit versus density. A steady decline in rotor efficiency is seen as the density is reduced. Density here is mostly a surrogate for Reynolds number, since for fixed thrust-weighted solidity, the chord at $r/R = 0.75$ varies very little with planform changes.

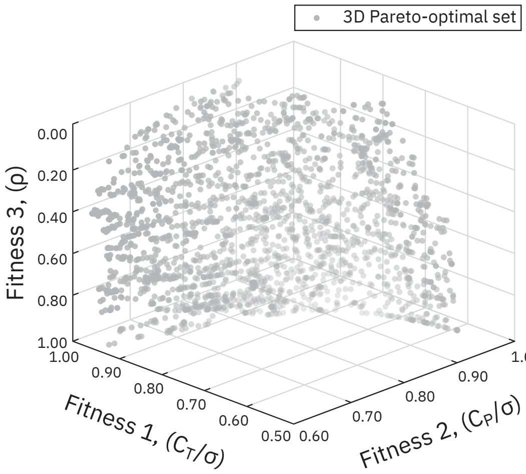

Figure 9. PO rotor set, $N = 6, \sigma = 0.25, 0.005 \leq \rho \leq 0.05$ kg/m^3.

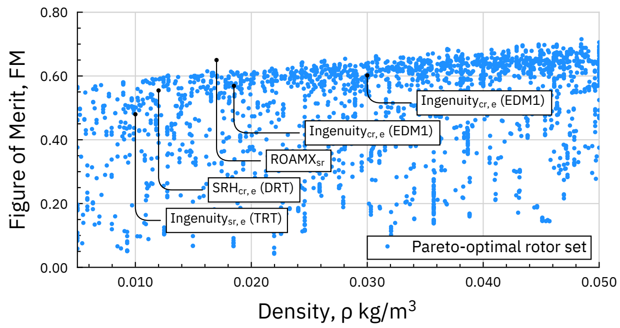

Figure 10. Figure of Merit versus density, $N = 6, \sigma = 0.25, 0.005 \leq \rho \leq 0.05$ kg/m^3.

Reference performance values are added from the EDM1, TRT, DRT test campaigns [18,19]. For the indicated densities, the maximum reported Figure of Merit values are plotted, irrespective of tip Mach number, for specific densities. Some of the reported performance figures are from coaxial rotor tests, rather than single isolated rotors, but the performance values are still considered valuable for context. The SRH rotor performance figures form the DRT test reflect the result of ELISA optimization of the coaxial rotor planform and twist distribution, using Ingenuity's airfoils [5]. The estimated ROAMX rotor performance [5], as optimized using ELISA, is added for context of a fully converged design. This also presents the downside of the current approach: for an equal amount of computational time, a higher number of 'objectives' will reduce the convergence rate. Besides the ROAMX rotor, all reference performance figures are from rotors using conventional airfoil shapes [5,23].

The twist and planform for three example PO rotors are plotted in Figure 11, obtained by selecting the peak Figure of Merit rotors at three different density conditions. As expected, very little chord variation is observed outboard due to the constrained thrust-weight solidity. The optimization is an interplay between minimizing profile power, which favors the larger chords, and induced power, which generally favors higher aspect ratio blades. Chord increases in outboard regions where the highest gains in airfoil performance are possible (so far as allowed by the local Mach number, see Table 1) and are limited here both by possible induced power penalties or simply the solidity constraint driving a big part of the blade aspect ratio.

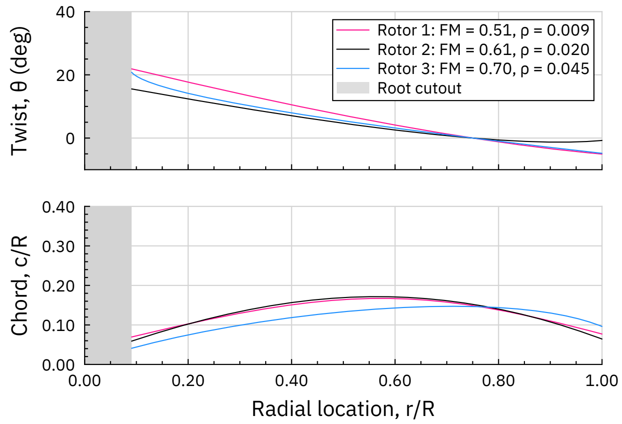

Figure 11. Rotor geometry trends for peak Figure of Merit at three densities, $N = 6, \sigma = 0.25$.

The airfoil profiles along the three rotor geometries (presented in Figure 11) are presented in Figure 12 for reference. Particularly noteworthy is the strong outboard camber reduction for rotor 1, compared to rotors 2 and 3.

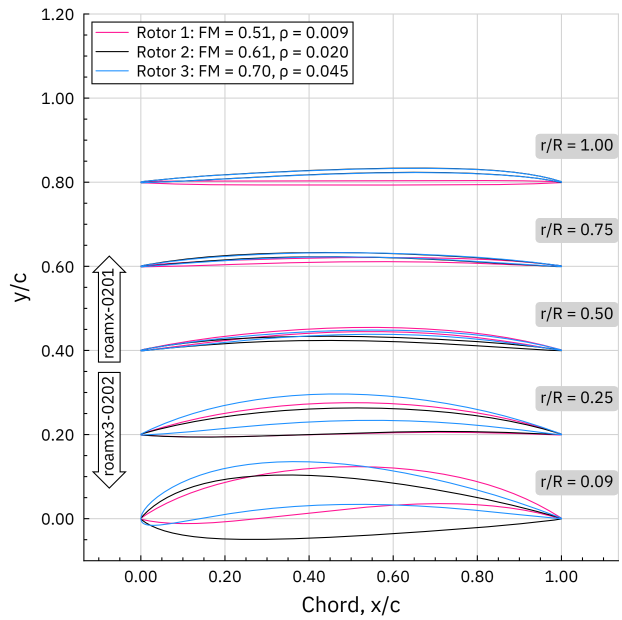

Figure 12. Airfoil geometry for rotors 1-3.

The root profile for Rotor 2 is likely a case of low sensitivity to poor aerodynamic coefficients on rotor performance due to the very low dynamic pressures at the blade roots, as well as the reduced fidelity of the PO airfoil set due to its reduced priority in the set, as can be inferred from the lower number of inboard PO airfoils in Table 1. The flow fields for rotors 1-3 at $r/R = 0.25$ ($t/c \geq 0.05$) are presented in Figure 13, Figure 14, and Figure 15, respectively.

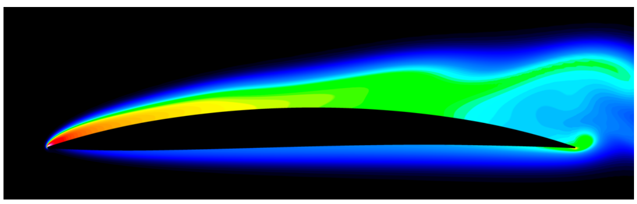

Figure 13. Instantaneous flow field for rotor 1 $r/R = 0.25$, $Re = 2{,}512$ (entropy measure s1).

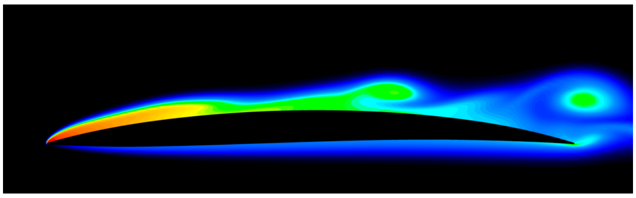

Figure 14. Instantaneous flow field for rotor 2 $r/R = 0.25$, $Re = 5{,}829$ (entropy measure s1).

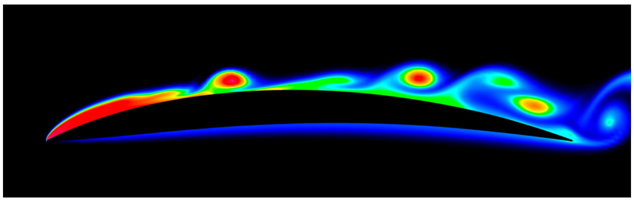

Figure 15. Instantaneous flow field for rotor 3 $r/R = 0.25$, $Re = 10{,}771$ (entropy measure s1).

The drastic change in flow field that accompanies the Reynolds number variation due to the density changes can be seen in the flow fields, clearly indicating the progressively larger scales of the unsteady structures at lower Reynolds numbers, with corresponding penalties in airfoil performance, as demonstrated in Table 3.

Table 3. Inboard mean airfoil performance for rotors 1-3, $r/R = 0.25, t/c \geq 0.05$.

Rotor	α (°)	Re	c_l	c_d	c_l/c_d
1	10	2,512	0.865	0.1333	6.49
2	7	5,829	0.811	0.0726	11.17
3	8	10,771	1.286	0.0898	14.32

Rotor Optimization without Solidity Constraint

The optimization problem under consideration is at its core a non-dimensional one, where only airfoil and rotor geometry are varied. The objective is to maximize the rotor thrust coefficient, C_T, (and Figure of Merit) while minimizing the rotor power coefficient, C_P, for a set tip Mach number and Reynolds number (at $r/R = 0.75$) and for a fixed solidity. However, thrust-weighted solidity can be considered a design parameter at the system level.

This chapter relaxes the constraints of the previous rotor optimization. The rotor solidities are now unconstrained, and optimizations are run for varying blade numbers ($3 \leq N \leq 7$). The blade number is limited to a maximum of $N = 7$ because at higher blade numbers the geometric constraints (see Table 2) start to strongly limit the inboard blade planform.

Figure 16 shows the PO rotor sets expressed as Figure of Merit as function of blade loading and density. As expected, the PO Figure of Merit values increase with density. A clear distinction in the peak Figure of Merit per blade number value can be seen until around $N = 6$ is reached, as shown in Figure 17. The blade loading at which the peak Figure of Merit is obtained for a particular density is also seen to increasing with blade number, as illustrated in Figure 18.

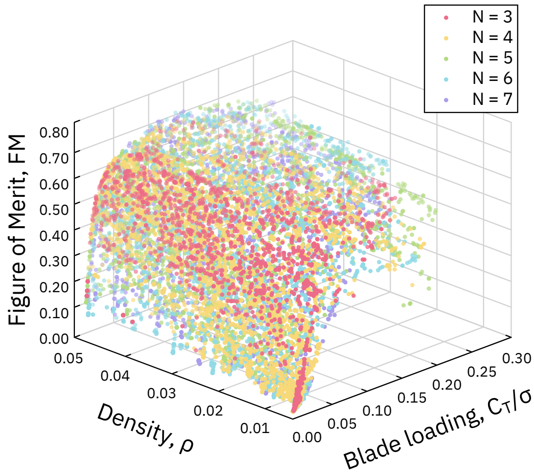

Figure 16. PO rotor sets, $3 \leq N \leq 7, 0.005 \leq \rho \leq 0.05$ kg/m^3.

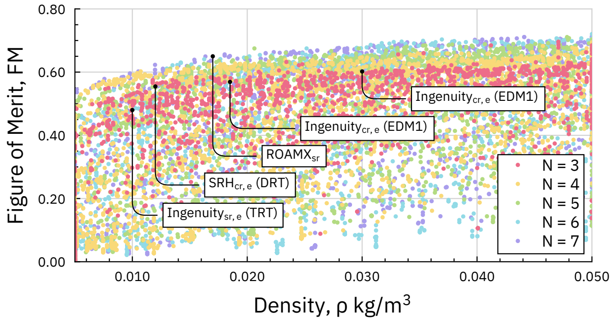

Figure 17. PO rotor sets highlighting Figure of Merit versus density, $3 \leq N \leq 7, 0.005 \leq \rho \leq 0.05$ kg/m^3.

Ignoring solidity, the maximum Figure of Merit values for Ingenuity class rotors (using unconventional airfoils) show slight increases compared to the fixed solidity and blade number optimization, as depicted in Figure 10.

Figure 18 further demonstrates that the blade loading at which peak Figure of Merit is reached generally increases with blade number. It is important to stress that these are single design points and do not provide insights into the stall behavior of these rotor geometries.

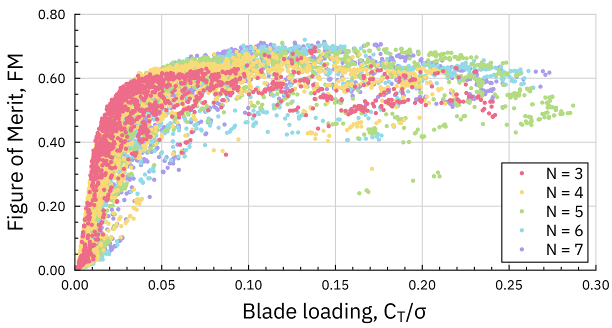

Figure 18. PO rotor sets highlighting Figure of Merit versus blade loading for $3 \leq N \leq 7, 0.005 \leq \rho \leq 0.05$ kg/m^3.

Figure 19 shows the PO rotor set Figure of Merit (for $FM \geq 0.50$) as function of each rotor's thrust-weighted solidity.

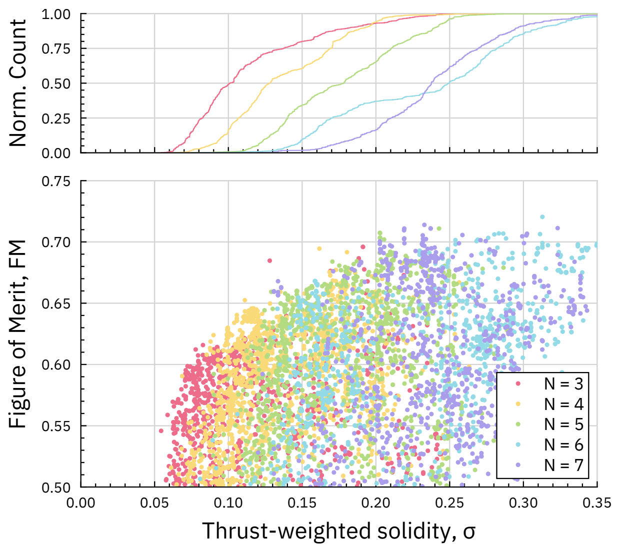

Figure 19. PO sets limited to $FM \geq 0.50$ highlighting Figure of Merit versus solidity for $3 \leq N \leq 7$.

The upper graph displays the cumulative normalized rotor count for each rotor geometry, corresponding to the lower graph. For low solidity values, rotors with a lower blade number can achieve the highest Figure of Merit values. This is because a larger chord for the same solidity can maximize Reynolds number, thereby reducing rotor profile power. However, an excessively large chord will increase induced power. A balance is evident in the PO rotor sets, with clear increase in solidity with blade number for the PO rotor sets.

To investigate the variation in blade planform, the peak Figure of Merit rotor geometries are extracted for a range of solidities, $0.100 \leq \sigma \leq 0.300$. Figure 20 displays the planform and twist distributions for each rotor. The corresponding solidity ratios and detailed rotor performance for each configuration are provide in Table 4.

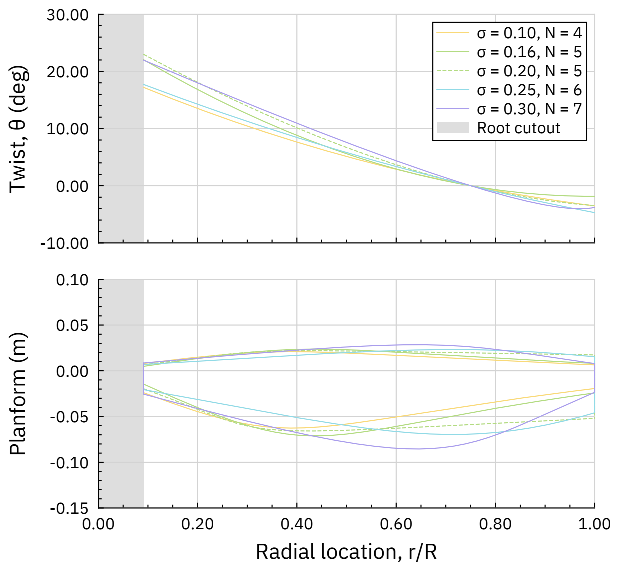

Figure 20. Rotor geometry trends for peak Figure of Merit, $0.100 \leq \sigma \leq 0.300$.

Table 4. Rotor performance trends for peak Figure of Merit, $0.100 \leq \sigma \leq 0.300$.

N	σ	ρ (kg/m^3)	C_T/σ	FM
4	0.104	0.047	0.054	0.63
5	0.155	0.047	0.074	0.66
5	0.203	0.048	0.168	0.71
6	0.254	0.048	0.115	0.70
7	0.302	0.043	0.176	0.71

Flow Regime Across Rotor Blade

Figure 21 shows the dataset presented in Figure 17, but only the rotor geometries are highlighted (colored) if anywhere on the rotor the continuum assumption could have been violated.

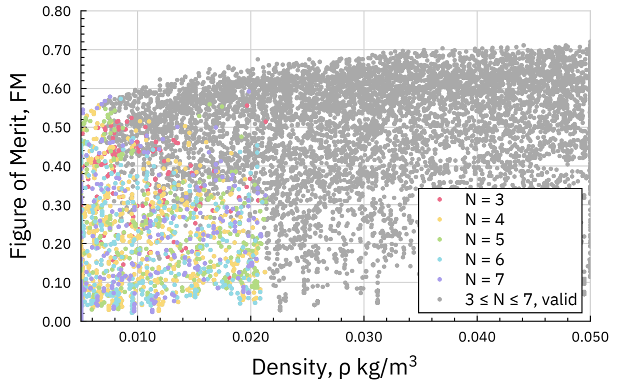

Figure 21. Continuum flow violations in PO rotor set for $3 \leq N \leq 7$.

Irrespective of rotor solidity and blade number, continuum flow physics could become invalid for rotors in the PO rotor set starting at around $\rho \leq 0.020$. Figure 22 shows an example rotor planform with a highlighted region where the threshold in Eq. (3) is violated.

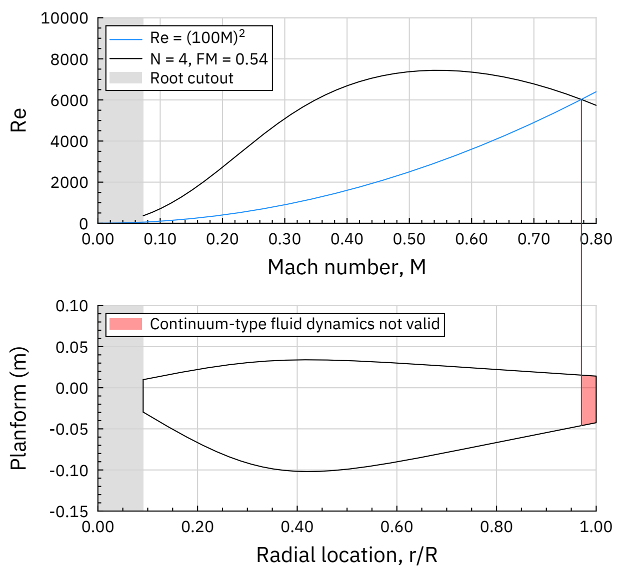

Figure 22. Continuum flow assumption violation for example rotor with $N = 0.006$, $FM = 0.54$, at $\rho = 0.006$.

While the transition from continuum flow physics to full rarefied flow is gradual [7], it is still important to keep track of the Reynolds and Mach number ratios for rotor design at low densities for Mars rotorcraft exploration.

CONCLUDING REMARKS

The main conclusions for this work are summarized here.

1. Upgrades to the Evolutionary aLgorithm for Iterative Studies of Aeromechanics (ELISA) were presented. The upgrades allow for Reynolds number variation during the airfoil optimization phase, and density variation during the rotor optimization phase.
2. Pareto-optimal (PO) rotor sets were presented for constrained and free solidities. These results provided an idea of the attainable Figure of Merit values across the practical density range for Mars rotorcraft exploration.
3. A study varying blade number showed the performance impact on the PO rotor set of different blade number-solidity combinations. Higher blade number, higher solidity rotors were seen to generally provide a higher Figure of Merit at higher blade loading values, for a density range $0.005 \leq \rho \leq 0.05$ kg/m^3 and rotor radius $R = 0.605$ m.

FUTURE WORK

In contrast to Earth-based rotorcraft, Mars rotorcraft generally are bound by a strict rotor radius constraint. Besides airfoil and rotor geometry investigations, optimization at much higher solidity values will be investigated to explore what the performance penalties will be for increased rotor thrust on Mars.

ACKNOWLEDGMENTS

The research of Witold J. F. Koning, B. Natalia Perez Perez, and Haley Cummings is made possible by the NASA FY21 Space Technology Mission Directorate Early Career Initiative Project "Rotor Optimization for the Advancement of Mars eXploration." The authors would like to acknowledge the support of William Warmbrodt and Larry Hogle during this research. Kristen Kallstrom, Shannah Withrow-Maser, and Sesi Kottapalli are thanked for their feedback in reviewing this paper. Resources supporting this work were provided by the NASA High-End Computing Program through the NASA Advanced Supercomputing Division at Ames Research Center.

REFERENCES

[1] Koning, W. J. F., Romander, E. A., and Johnson, W., "Optimization of Low Reynolds Number Airfoils for Martian Rotor Applications Using an Evolutionary Algorithm," AIAA Science and Technology Forum and Exposition (AIAA SciTech), AIAA Paper 2020-0084, 2020, Orlando, FL, U.S.A., January 2020. https://doi.org/https://doi.org/10.2514/6.2020-0084

[2] Koning, W. J. F., Romander, E. A., and Johnson, W., "Performance Optimization of Plate Airfoils for Martian Rotor Applications Using a Genetic Algorithm," 45th European Rotorcraft Forum, Warsaw, Poland, September 2019.

[3] Johnson, W., Withrow-Maser, S., Young, L., Malpica, C., Koning, W. J. F., Kaung, W., Fehler, M., Tuano, A., Chan, A., Datta, A., Chi, C., Lumba, R., Escobar, D., Balaram, J., Tzanetos, T., and Grip, H. F., "Mars Science Helicopter Conceptual Design," Moffett Field, CA, U.S.A., NASA/TM–2020-220485, 2020.

[4] Chi, C., Lumba, R., Su Jung, Y., and Datta, A., "Aeromechanical Analysis of a Next-Generation Mars Hexacopter Rotor," Journal of Aircraft, Vol. 59, No. 6, 2022, pp. 1463–1477. https://doi.org/10.2514/1.C036739

[5] Koning, W. J. F., Perez, B. N. P., Cummings, H. V, Romander, E. A., and Johnson, W., "ELISA: A Tool for Optimization of Rotor Hover Performance at Low Reynolds Number in the Mars Atmosphere," Vertical Flight Society Sixth Decennial Aeromechanics Specialists' Conference, Santa Clara, CA, U.S.A., February 2024.

[6] Sobieczky, H., "Parametric Airfoils and Wings," *Recent development of aerodynamic design methodologies: inverse design and optimization*, Springer, 1999, pp. 71–87.

[7] Hoerner, S. F., "Fluid-Dynamic Drag: Practical Information on Aerodynamic Drag and Hydrodynamic Resistance," Hoerner Fluid Dynamics, 1965.

[8] Nichols, R. H., and Buning, P. G. "User's Manual for OVERFLOW 2.2." Langley Research Center, Hampton, VA, 2008.

[9] Pulliam, T. H., "High Order Accurate Finite-Difference Methods: As Seen in OVERFLOW." 20th AIAA Computational Fluid Dynamics Conference, AIAA Paper 2011-3851, Honolulu, HI, U.S.A., June 2011.

[10] Tramel, R., Nichols, R., and Buning, P., "Addition of Improved Shock-Capturing Schemes to OVERFLOW 2.1." 19th AIAA Computational Fluid Dynamics, AIAA Paper 2009-3988, San Antonio, TX, U.S.A., June 2009. https://doi.org/doi:10.2514/6.2009-3988

[11] Pulliam, T. H. "Time Accuracy and the Use of Implicit Methods." 11th AIAA Computational Fluid Dynamics Conference, AIAA Paper 1993-3360, Orlando, FL, U.S.A., July 1993. https://doi.org/10.2514/6.1993-3360.

[12] Pandya, S., Venkateswaran, S., and Pulliam, T. H. "Implementation of Preconditioned Dual-Time Procedures in OVERFLOW." AIAA 41st Aerospace Sciences Meeting, AIAA Paper 2003-0072, Reno, NV, U.S.A., Jan. 2003. https://doi.org/10.2514/6.2003-72.

[13] Koning, W. J. F., Romander, E. A., Cummings, H. V., Perez Perez, B. N., and Buning, P. G. "On Improved Understanding of Airfoil Performance Evaluation Methods at Low Reynolds Numbers." *Journal of Aircraft*, Vol. 60, No. 3, May 2023. https://doi.org/10.2514/1.C037023

[14] Bergmann, M., Morsbach, C., Ashcroft, G., and Kügeler, E., "Statistical Error Estimation Methods for EngineeringRelevant Quantities from Scale-Resolving Simulations," *Journal of Turbomachinery*, Vol. 144, No. 3, 2022. https://doi.org/10.1115/1.4052402

[15] Koning, W. J. F., Allan, B. G., Romander, E. A., and Johnson, W., "Comparing 3D and 2D CFD for Mars Helicopter Ingenuity Rotor Performance Prediction," 49th European Rotorcraft Forum, Bückeburg, Germany, September 2023.

[16] Johnson, W. "Rotorcraft Aerodynamics Models for a Comprehensive Analysis." AHS International 54th Annual Forum & Technology Display, Fairfax, VA, U.S.A., 1998.

[17] Koning, W. J. F., Romander, E. A., and Johnson, W., "Low Reynolds Number Airfoil Evaluation for the Mars Helicopter Rotor," AHS International 74th Annual Forum & Technology Display, Phoenix, AZ, U.S.A., May 2018.

[18] Withrow-Maser, S., Johnson, W., Tzanetos, T., Grip, H., Koning, W., Schatzman, N., Young, L., Chan, A., Ruan, A., and Cummings, H., "Mars Sample Recovery Helicopter: Rotorcraft to Retrieve the First Samples from the Martian Surface," Vertical Flight Society's 79th Annual Forum & Technology Display, West Palm Beach, FL, U.S.A., May 2023.

[19] Schatzman, N., Chan, A., Fillman, M., Meyn, L., Gehlot, V., Glazebrook, K., Santillan, D., and Ridland, P., "Performance Analysis and Data Processing for the Mars Sample Recovery Helicopter in the Jet Propulsion Laboratory 25-Ft Space Simulator," Vertical Flight Society's 80th Annual Forum & Technology Display, Montreal, Quebec, Canada, May 2024.

[20] Kallstrom, K., Weist, L., Schatzman, N., Shirazi, D., Dominguez, M., and Young, L., "PlanetarY Telemetric Helicopter for Investigation and Analysis (PYTHIA): A Rotorcraft for Martian Lava Tube Exploration," Vertical Flight Society Sixth Decennial Aeromechanics Specialists' Conference, Santa Clara, CA, February 2024.

[21] Schatzman, N., Dominguez, M., Lee, P., and Young, L., "LILI (Long-Term Ice-Field Levitating Investigator): Mars Aerial and Ground Explorer for Martian Polar Regions," VFS Aeromechanics for Advanced Vertical Flight Technical Meeting, San Jose, CA, Jan 2022.

[22] Mier-Hicks, F., Grip, H. F., Kalantari, A., Moreland, S., Pipenberg, B., Keennon, M., Canham, T. K., Pauken, M., Decrossas, E., and Tzanetos, T. "Sample Recovery Helicopter." 2023 IEEE Aerospace Conference, Big Sky, MT, U.S.A., 2023. doi: 10.1109/AERO55745.2023.10115951.

[23] Koning, W. J. F., and Dominguez, M., "Mars Helicopter Ingenuity Rotor Geometry," NASA/TM–20240001510, February 2024.